SIAM J. SCI. COMPUT.
Vol. 41, No. 1, pp. B181–B204

SHAPE OPTIMIZATION OF A COMPRESSION DRIVER PHASE PLUG*

ANDERS BERNLAND†, EDDIE WADBRO†, AND MARTIN BERGGREN†

Abstract. A compression driver is an electro-acoustic transducer with considerably higher efficiency than direct radiating loudspeakers, thanks to the increased radiation resistance caused by a large vibrating diaphragm placed in a compression chamber with small openings. The transition section between compression chamber and output waveguide, the phase plug, must be carefully designed to avoid irregularities in the output sound pressure level (SPL) as a function of frequency. Here we present a shape optimization method based on an implicit level-set description and adjoint sensitivity analysis, which enables a large number of design parameters and vast design freedom. The CutFEM approach, a fictitious domain finite element method, removes the need for mesh updates and makes the method robust and computationally inexpensive. Numerical experiments for a generic annular diaphragm compression driver are presented, with optimized designs showing only minor frequency irregularities. Two different objective functions are considered: one for maximum SPL and one where the SPL is fitted to that of a hypothetical ideal design; the latter approach is found to be more effective in reducing irregularities. Visco-thermal boundary-layer losses are included in a post-processing step, and, though the influence of losses is clearly noticeable, the overall performance is similar and the optimized designs still outperform the original design.

Key words. shape optimization, level set, CutFEM, Helmholtz equation, electro-acoustic transducer

AMS subject classifications. 65K10, 35J05, 65N30, 65N85

DOI. 10.1137/18M1175768

1. Introduction.

A *compression driver* is an electro-acoustic transducer commonly used to feed horns to cover the mid- to high-frequency spectra in applications where high acoustic power is needed, such as public address systems. In a direct radiating loudspeaker, the low radiation resistance at most of its operational frequency range causes a loading mismatch between the air and the vibrating membrane. This mismatch limits the maximum achievable efficiency, and in practice it is hard to achieve more than 1% efficiency with this setup [31, p. 46]. To increase the radiation resistance, the vibrating membrane, or diaphragm, in a compression driver is placed in a shallow chamber, from which the sound can exit only through a number of narrow slits. With a high quotient, typically around 10, of diaphragm area to total exit area (the *compression ratio*), a compression driver can achieve far higher efficiency than direct radiating loudspeakers. The sound exiting the compression chamber propagates through narrow channels, ending in a circular duct to which an acoustic horn or waveguide can be mounted. The transition region, the *phase plug*, must be carefully designed to avoid response irregularities, which cause poor perceived sound quality. Phase plug design has been considered in a number of previous studies [13, 14, 18, 32, 33, 36, 42]; nevertheless, we believe that there is great potential in

*Submitted to the journal's Computational Methods in Science and Engineering section April 17, 2018; accepted for publication (in revised form) December 27, 2018; published electronically February 26, 2019.

http://www.siam.org/journals/sisc/41-1/M117576.html

Funding: This work was supported by the Swedish Foundation for Strategic Research contract/grant AM13-0029, Swedish Research Council contract/grant 621-2013-3706, and eSSENCE (a strategic collaborative eScience program funded by the Swedish Research Council).

†Department of Computing Science, Umeå University, SE-901 87 Umeå, Sweden (anders.bernland@cs.umu.se, eddie.wadbro@cs.umu.se, martin.berggren@cs.umu.se).

applying numerical optimization algorithms to compression driver phase plug design, something that appears not to have been investigated properly.

Today, it is more or less standard to use numerical optimization in design problems within, for example, elasticity, fluid mechanics, electromagnetics, and acoustics [10]. Typically, a combination of geometry discretization, numerical modeling of the underlying physics, and optimization algorithms is chosen to efficiently explore the design space in search of an optimal solution. A clear distinction exists between gradient-free [28] and gradient-based [35] optimization algorithms, and, for the latter, the cost of computing the discrete shape sensitivities is crucial. With adjoint methods, the computational cost does not increase with the number of design parameters (as long as the computational mesh remains the same), a fact that enables optimization over a larger set of parameters and in practice makes the difference between merely improving an already existing design and finding a conceptually new one.

Geometry discretization on fixed background meshes has become increasingly popular in the last decade, since mesh updates can be costly, can harm the convergence of the optimization, and are not always robust. Fixed mesh methods, usually labeled fictitious domain, domain embedding, or immersed boundary methods, are used not only in design problems, but also when traditional body fitted meshes are computationally expensive to construct or where the geometry is evolving over time. Finite element methods on fixed meshes appear under names such as GFEM/XFEM [16], CutFEM [7], CDFEM [29], and IGFEM [37], to name a few. In a pioneering study concerning stress minimization in filets, Van Miegroet and Duysinx [40] combined XFEM with a level-set description, and similar methods were refined in several publications [24, 26, 41, 43]; see also the reviews in [5, 17, 39].

Shape and topology optimization of acoustic horns, to achieve improved impedance matching, smoother frequency response, or certain directivity properties, has received considerable attention [1, 2, 15, 21, 25, 27, 30, 34]. In a previous study [4], we optimized an acoustic horn for impedance matching by using CutFEM and a level-set description, an approach that was found to be robust and computationally inexpensive. Furthermore, the optimized horns showed unexpected subwavelength structures, not seen in previous analyses, that served to improve the matching properties; such features could be captured due to the large design freedom given by the parametrization in terms of the filtered nodal values of the discretized level set. Another advantage of the fixed-mesh optimization scheme was that the discrete shape sensitivities could be computed exactly (up to round-off) by boundary integrals; when instead optimizing with a boundary-fitted mesh and mesh deformations, the discrete sensitivities must be computed by volume integrals to avoid consistency errors [3]. There does not seem to be much previous work regarding acoustic shape optimization on fixed finite element meshes, but Legay's study [22] on noise reduction by optimal placement of structures within an acoustic cavity should be mentioned.

In this paper, we consider shape optimization of annular channel phase plugs using CutFEM and a level-set description similar to the approach we used for horn design in [4]; the starting design of the generic compression driver can be found in Figure 1. Section 2 gives some more detailed background regarding compression drivers. Section 3 describes the acoustic modeling with the Helmholtz equation, in combination with a full electro-mechanical model for the motion of the diaphragm, as well as the geometry discretization on the fixed mesh and the objective functions and sensitivity analysis needed for the optimization algorithm. Optimization results are presented in section 4, and the influence of viscous and thermal boundary-layer losses are also taken into account. Finally, conclusions can be found in section 5.

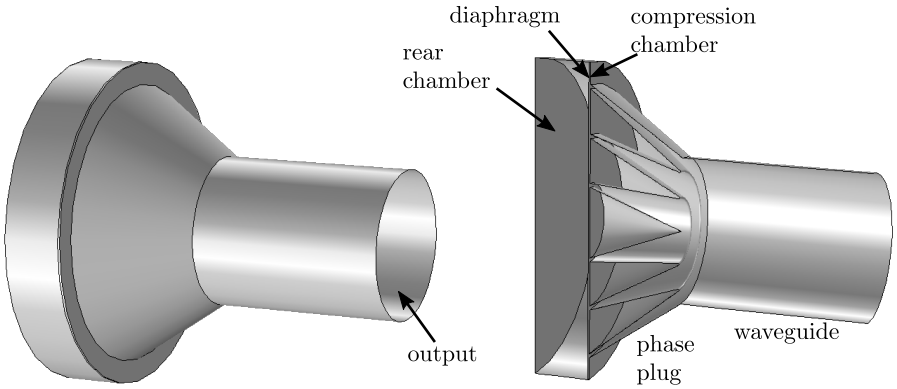

FIG. 1. *The original design of the generic compression driver considered.*

2. Compression driver phase plugs. The acoustic power in a compression chamber is generated by a large vibrating diaphragm, typically made of a thin foil of aluminium or titanium to be light but rigid, and suspended as to allow for axial motion [31]. To increase rigidity, the diaphragm is commonly curved into a dome shape, but there are also drivers with cone or flat annular ring diaphragms [42]. The diaphragm is set in motion by an alternating current in the voice coil, wound onto a rigid former attached to the diaphragm, and immersed in the radial magnetic field created by a ring magnet. The diameter of the voice coil, typically 1–4 inches, is used to denote the size of the driver.

The idea of combining a large diaphragm and a small horn throat to increase radiation resistance and efficiency was first presented in 1924 by Hanna and Slepian [19], who connected the compression chamber directly to the horn throat. While improving the impedance match at moderately high frequencies, this simple setup suffers from radial resonances in the compression chamber, which cause frequency response irregularities and limit the upper operational frequency. Wente and Thuras [44] introduced a phase plug with one annular channel between the compression chamber and the horn throat, and could thus partly avoid the radial resonances and push the usable frequency limit further up.

Smith's 1953 publication [36] has had a profound impact on compression driver phase plugs; for a cylindrical compression chamber with a rigid piston, he showed that the use of N annular channels could suppress the first N radial modes in the compression chamber, and he derived design guidelines for accomplishing this. The Nth radial mode, given by the Nth cylindrical Bessel function, has N pressure nodes within the cavity, and Smith argued that the mode will not be excited if the channel entrances are placed at these locations. Furthermore, the areas of the channel entrances, the slits, give N more degrees of freedom. Avoiding excitation of modes $1, 2, \ldots, N-1$ gives $N-1$ conditions, which are used to set the relative area of slits. Finally, the desired compression ratio, defined as the quotient of the diaphragm area and total slit area, gives an additional condition required to uniquely determine the slit absolute areas. In addition to Smith's original work, detailed derivations of Smith's guidelines have been carried out by Dodd and Oclee-Brown [14, 31]. Similar derivations are therefore omitted here, but the results for a three channel phase plug can be found in

Table 1.

TABLE 1
Smith's guidelines for the locations of the channel entrances (relative chamber radius r) and their relative widths for a phase plug with three annular channels [36].

Location	Relative width
$0.238r$	1
$0.543r$	1.025
$0.853r$	1.065

Smith's design guidelines rely on a few assumptions that need to be highlighted. First, Smith assumes a flat, cylindrical, compression chamber. Dodd and Oclee-Brown derive modified guidelines for a spherical-cap chamber using a decomposition in spherical coordinates [14], and a methodology for more general geometries based on finite element calculation of the chamber eigenvalues [32], results which can also be found in Oclee-Brown's thesis [31]. Voishvillo derives similar guidelines for an annular ring compression chamber [42].

Second, the piston is assumed to be rigid, whereas a real compression driver diaphragm can break up at high frequencies, a phenomenon that results in frequency irregularities. Christensen and Skov [8] couple structural and acoustic modeling in a simulation of a 4-inch beryllium diaphragm compression driver. They note that the break-up occurs at high frequencies and is not critical to the usable bandwidth of the driver in this case, but predict it to be more critical with an aluminum or titanium diaphragm. Oclee-Brown [31] uses laser scans to show that break-up does occur for a 3-inch driver at 12.8 kHz. He argues that the driver response is not limited by the break-up if the nonrigid structural modes do not excite the acoustic modes of the cavity and optimizes a cavity shape with the aim of meeting this criterion. Voishvillo [42] shows laser scan measurements of break-up for a flat annular-ring diaphragm and proposes a meandering channel entrance to "smear out" the irregularities caused by structural and acoustical modes.

Finally, Smith's design guidelines rely on the assumption that the acoustic velocities are equal at the channel entrances. This is valid for separated channels of constant area, each infinitely long or terminated with no reflection, but not necessarily for channels joining at the exit in a real compression driver phase plug. The mounting of a phase plug to the exits, several times longer than the wavelength of the highest frequency to be used, gives rise to a complex acoustical system, and the phase plug channel paths need to be carefully designed to avoid internal resonances. Dodd and Oclee-Brown [12, 14, 31] suggest curving the path of the channels to make them equal in length and show that such a design creates a smoother frequency response.

Notwithstanding the favorable results that guidelines and engineering know-how can provide, it is our opinion that compression driver phase plug design is a problem well suited for boundary shape optimization, and that such a study is timely. We focus on the shape of the phase plug channel paths and therefore consider a flat, cylindrical compression chamber and restrict our attention to frequencies where diaphragm break-up can be expected to be noncritical. The driver is connected to a semi-infinite waveguide, and the walls of the chamber, phase plug, and waveguide are also assumed stiff. The starting point is the generic compression driver design in Figure 1, where Smith's guidelines have been used.

Viscous and thermal boundary-layer losses can have a profound impact on compression driver performance, due to the high surface to volume ratio of the compression

chamber and phase plug [8]. A model where the acoustic losses are accounted for, by solving the linearized, compressible Navier–Stokes equations, is computationally much more expensive than disregarding losses and solving the Helmholtz equation. Therefore, acoustic losses are neglected during the optimization but taken into account in a post-processing step.

3. Problem statement.

3.1. Acoustical problem. We assume that the acoustic pressure P satisfies the linear wave equation, and we consider time-harmonic solutions $P(\boldsymbol{x},t) = \mathrm{Re}(p(\boldsymbol{x})\mathrm{e}^{\mathrm{i}\omega t})$. Here Re denotes the real part, p is the complex amplitude function, $\boldsymbol{x}$ is the spatial coordinate, i is the imaginary unit, ω is the angular frequency, and t denotes time. The diaphragm Γ_{m} separates the compression chamber in front of it from the rear chamber and thus divides the computational domain in two: the union of compression chamber, phase plug, and waveguide, denoted Ω, and the rear chamber, denoted Ω_{b}. The boundary problems for p in Ω and Ω_{b} are

$$\Delta p + k^2 p = 0 \qquad \text{in } \Omega \text{ and } \Omega_{\mathrm{b}}, \tag{3.1a}$$

$$\frac{\partial p}{\partial n} = \mathrm{i}kc\rho_0 u_{\mathrm{m}} \qquad \text{on } \Gamma_{\mathrm{m}}, \tag{3.1b}$$

$$\mathrm{i}kp + \frac{\partial p}{\partial n} = 0 \qquad \text{on } \Gamma_{\mathrm{out}}, \tag{3.1c}$$

$$\frac{\partial p}{\partial n} = 0 \qquad \text{on } \Gamma \setminus (\Gamma_{\mathrm{out}} \cup \Gamma_{\mathrm{m}}), \tag{3.1d}$$

where $k = \omega/c$ is the (isentropic) wavenumber, c is the (isentropic) speed of sound, ρ_0 is the static density of air, $\partial/\partial n = \hat{\boldsymbol{n}} \cdot \nabla$ is the normal derivative, and $\hat{\boldsymbol{n}}$ is the unit normal, which is directed outwards with respect to Ω. For clarity, the acoustic pressure in the back chamber Ω_{b} will be denoted p_{b} from now on. Figure 2 shows a cut through the symmetry plane of the rotationally symmetric geometry, along with definitions of the boundaries. The waveguide is modeled as infinitely long by applying boundary condition (3.1c) on its right end Γ_{out}; the boundary condition absorbs planar modes, and nonplanar modes can be neglected for the frequencies considered here. The boundary condition on the diaphragm Γ_{m} is a given velocity u_{m}.

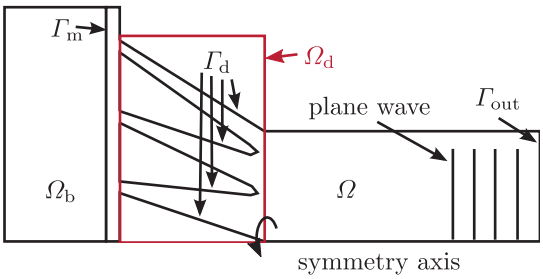

FIG. 2. *The symmetry plane of the rotationally symmetric compression driver of Figure* 1. *The three-dimensional domains Ω and Ω_{b} are obtained by rotation around the symmetry axis. The design domain Ω_{d} covers the area where the design boundary Γ_{d} is allowed to take its path. Note that the figure is not to scale.*

The diaphragm is set in motion by a coil in a magnetic field, where the coil and diaphragm velocities are assumed equal and denoted by u_{m}. The driver's motor

system is

$$BlI - \int_{\Gamma_\mathrm{m}} [\![p]\!] \,\mathrm{d}\Gamma - Z_\mathrm{m} u_\mathrm{m} = 0, \tag{3.2a}$$

$$IZ_\mathrm{e} + Blu_\mathrm{m} = V, \tag{3.2b}$$

where Bl is the force factor (given by the product of the magnetic flux density B and coil length l), I is the current through the voice coil, V is the applied electric voltage, Z_e is the electric impedance of the circuit, and the mechanical impedance is given by

$$Z_\mathrm{m} = R_\mathrm{m} + \mathrm{i}\left(M_\mathrm{m}\omega - \frac{1}{C_\mathrm{m}\omega}\right), \tag{3.3}$$

where R_m is the mechanical resistance, M_m is the moving mass, and C_m is the suspension compliance. The second term in equation (3.2a) is a force on the diaphragm due to the difference in pressure on its two sides, where $[\![p]\!] = p|_{\Gamma_\mathrm{m}} - p_\mathrm{b}|_{\Gamma_\mathrm{m}}$ and p (p_b) denotes the pressure in Ω (Ω_b), respectively.

Finally, we state the variational formulation of boundary value problem (3.1), which is

$$\begin{aligned} &\text{Find } p \in H^1(\Omega), u_\mathrm{m} \in \mathbb{C}, \text{ and } I \in \mathbb{C}, \text{ such that} \\ &A(p,q) = L(q) \quad \forall q \in H^1(\Omega), \\ &\text{and such that the circuit equations (3.2) are satisfied,} \end{aligned} \tag{3.4}$$

where

$$A(p,q) = \int_\Omega \nabla q \cdot \nabla p \,\mathrm{d}\Omega - k^2 \int_\Omega qp \,\mathrm{d}\Omega + \mathrm{i}k \int_{\Gamma_\mathrm{out}} qp \,\mathrm{d}\Gamma, \tag{3.5a}$$

$$L(q) = \mathrm{i}kc\rho_0 u_\mathrm{m} \int_{\Gamma_\mathrm{m}} q \,\mathrm{d}\Gamma. \tag{3.5b}$$

The Sobolev space $H^1(\Omega)$ is the space of square integrable functions of Ω for which all partial derivatives of first order are also square integrable.

The rear chamber Ω_b can be accounted for by modifying the mechanical impedance Z_m with an additional frequency dependent compliance term. Since we assume that the piston moves rigidly, the pressure in Ω_b depends only on the distance z from the rear wall. When the depth l_b of Ω_b is less than half a wavelength, there is no axial resonance in Ω_b and the pressure there is

$$p_\mathrm{b} = \mathrm{i}c\rho_0 u_\mathrm{m} \frac{\cos(kz)}{\sin(kl_\mathrm{b})}, \tag{3.6}$$

where $z = 0$ at the rear wall and $z = l_\mathrm{b}$ at Γ_m. A direct differentiation shows that expression (3.6) satisfies boundary value problem (3.1) in Ω_b. Substituting expression (3.6) into circuit equation (3.2a), we find that

$$BlI - \int_{\Gamma_\mathrm{m}} p \,\mathrm{d}\Gamma - Z'_\mathrm{m} u_\mathrm{m} = 0, \tag{3.7}$$

where the adjusted mechanical impedance is

$$Z'_\mathrm{m} = Z_\mathrm{m} - \mathrm{i}c\rho_0 |\Gamma_\mathrm{m}| \cot(kl_\mathrm{b}), \tag{3.8}$$

in which $|\Gamma_{\mathrm{m}}|$ is the area of Γ_{m}.

Note that the unknowns in variational formulation (3.4) are p, u_{m}, and I, where u_{m} and I, for a given p, are given by the driver's motor system (3.2). If $B^2l^2+Z_{\mathrm{e}}Z'_{\mathrm{m}} \neq 0$, however, we can explicitly solve equations (3.2) for the driver motor system to arrive at the membrane velocity

$$u_{\mathrm{m}} = \frac{1}{B^2l^2 + Z_{\mathrm{e}}Z'_{\mathrm{m}}} \left(BlV - Z_{\mathrm{e}} \int_{\Gamma_{\mathrm{m}}} p \, \mathrm{d}\Gamma \right). \tag{3.9}$$

The assumption $B^2l^2+Z_{\mathrm{e}}Z'_{\mathrm{m}} \neq 0$ is related to a lack of resonances in the motor system and holds if, for example, there are losses, namely, $\operatorname{Re} Z_{\mathrm{e}} > 0$ or $\operatorname{Re} Z_{\mathrm{m}} = R_{\mathrm{m}} > 0$. Variational formulation (3.4) can then be rewritten as

$$\begin{aligned} &\text{Find } p \in H^1(\Omega) \text{ such that} \\ &A'(p,q) = L'(q) \quad \forall q \in H^1(\Omega), \end{aligned} \tag{3.10}$$

where

$$A'(p,q) = \int_\Omega \nabla q \cdot \nabla p \, \mathrm{d}\Omega - k^2 \int_\Omega qp \, \mathrm{d}\Omega + \mathrm{i}k \int_{\Gamma_{\mathrm{out}}} qp \, \mathrm{d}\Gamma + \frac{\mathrm{i}kc\rho_0}{Z_{\mathrm{eff}}} \int_{\Gamma_{\mathrm{m}}} q \, \mathrm{d}\Gamma \int_{\Gamma_{\mathrm{m}}} p \, \mathrm{d}\Gamma, \tag{3.11a}$$

$$L'(q) = \mathrm{i}kc\rho_0 \frac{Bl}{Z_{\mathrm{eff}} Z_{\mathrm{e}}} V \int_{\Gamma_{\mathrm{m}}} q \, \mathrm{d}\Gamma, \tag{3.11b}$$

in which we have introduced the effective impedance

$$Z_{\mathrm{eff}} = \frac{B^2l^2 + Z_{\mathrm{e}}Z'_{\mathrm{m}}}{Z_{\mathrm{e}}}. \tag{3.12}$$

Well-posedness of problem (3.10) is shown in Appendix A.

3.2. Optimization problem. Our aim is to design the phase plug to avoid irregularities and achieve a favorable output power over the frequency spectrum of operation. To this end, the shapes of the channels in the phase plug are optimized. A level-set function ϕ is used to define the edges of the channels, the design boundary Γ_{d}, as the points $\boldsymbol{x}$ where the level-set function vanishes, that is,

$$\Gamma_{\mathrm{d}} = \{\boldsymbol{x} : \phi(\boldsymbol{x}) = 0\}. \tag{3.13}$$

The level-set function is defined in the design domain Ω_{d} around the phase plug (see Figure 2) and such that $\boldsymbol{x}$ is in the interior of the domain Ω if $\phi(\boldsymbol{x}) < 0$. A straightforward choice of ϕ that fulfills (3.13) is the signed distance function, which for each $\boldsymbol{x}$ in $\mathbb{R}^3$ equals the minimum distance from $\boldsymbol{x}$ to a point on the boundary Γ_{d}.

The output power in the waveguide is determined from the acoustic pressure p at the right end of the waveguide, Γ_{out}, and, since there are no reflections, it is given by

$$P_{\mathrm{out}}(\phi,k) = \frac{1}{2\rho_0 c} \int_{\Gamma_{\mathrm{out}}} |p(k)|^2 \, \mathrm{d}\Gamma = \frac{1}{2\rho_0 c} |\Gamma_{\mathrm{out}}| |p^{\mathrm{out}}(k)|^2. \tag{3.14}$$

In the second equality we use that the pressure p for planar modes is constant on the boundary Γ_{out} and denote this constant p^{out}. Note that the pressure and output

power depend on the geometry of the phase plug, given by the level-set function ϕ, as well as on the wavenumber k and the electrical and mechanical parameters.

A straightforward goal is to maximize the sum of the output power over a discrete set of frequencies, in which case the objective function to be minimized can be defined as

$$J_{\max}(\phi) = \frac{1}{2N_k} \sum_{n=1}^{N_k} \frac{1}{|p^{\text{out}}(k_n)|^2}. \tag{3.15}$$

Another approach is to try to match the output power as a function of frequency to the function obtained with a reference solution, in this case chosen as the hypothetical ideal design with straight channels illustrated in Figure 3. Such a design, although useless for most practical purposes, does not exhibit any resonances and therefore serves well as a reference solution. The objective function to be minimized for this case is defined as

$$J_{\text{diff}}(\phi) = \frac{1}{2N_k} \sum_{n=1}^{N_k} |p^{\text{out}}(k_n) - p^{\text{out}}_{\text{ref}}(k_n)|^2. \tag{3.16}$$

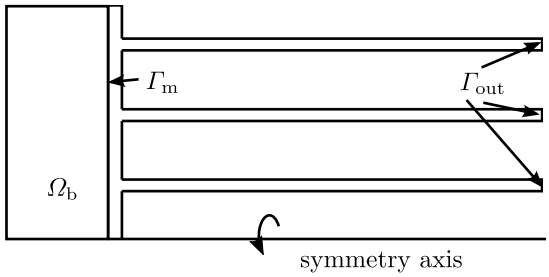

FIG. 3. *The restriction of the computational domain to the symmetry plane for the driver with straight channels, used to compute the reference solution* $p^{\text{out}}_{\text{ref}}$ *in objective function* (3.16). *Here the output boundary is not connected, and the output power* $p^{\text{out}}_{\text{ref}}$ *is defined as the sum of the power in each of the channels. Note that the figure is not to scale.*

Smoothing, filtering, and regularization approaches, which modify the optimization problem in one form or another, are routinely used in shape and topology optimization to counteract mesh dependence, improve the convergence rate, and promote smooth designs [39]. In our previous study of the acoustic horn [4], it was seen that a smoothing algorithm that served all three purposes was to optimize over the Laplacian of the level-set function. The method, which is similar to the one employed by Bängtsson, Noreland, and Berggren [1], is used in this paper as well. That is, the level-set function ϕ is given by the solution to the equation

$$\begin{cases} -\Delta\phi = \hat{\phi} & \text{in } \Omega_{\text{d}}, \\ \phi = \phi_0 & \text{on } \partial\Omega_{\text{d,D}}, \\ \frac{\partial\phi}{\partial n} = 0 & \text{on } \partial\Omega_{\text{d,N}}. \end{cases} \tag{3.17}$$

In the formulation of the optimization problem, the set $\hat{U}_{\text{ad}}$ of admissible functions $\hat{\phi}$ is chosen as the space of rotationally symmetric, square integrable functions, which implies that ϕ is in $H^2(\Omega_{\text{d}}) \subset C^0(\overline{\Omega}_{\text{d}})$ for smooth or convex Ω_{d}.

The position and relative area of the channel entrances are chosen according to Table 1, in order not to excite the radial modes of the compression chamber, as discussed in section 2. The total area of the channel entrances is chosen according to the desired compression ratio. These channel positions and opening areas are kept constant throughout the optimization, enforced by the constant level-set boundary values ϕ_0. To give more design freedom near the interface to the waveguide, the homogeneous Neumann boundary condition $\partial\phi/\partial n = 0$ is applied there.

Tikhonov regularization is sometimes used in level-set based optimization methods [39] to control the norm of the solution and was found in [4] to result in optimized acoustic horns with lower curvature. The addition of Tikhonov regularization also improved the convergence rate of the optimization algorithm more than just using the level-set smoothing (3.17). In this study, the Tikhonov term

$$J_\epsilon(\hat{\phi}) = \frac{1}{2}\int_{\Omega_\mathrm{d}} (\hat{\phi} - \hat{\phi}_0)^2 \,\mathrm{d}\Omega \tag{3.18}$$

is added to yield the objective function

$$J(\hat{\phi}) = J_\mathrm{obj}(\phi(\hat{\phi})) + \epsilon_\mathrm{r} J_\epsilon(\hat{\phi}). \tag{3.19}$$

Here $\hat{\phi}_0$ denotes the auxiliary function for the starting design, and the unregularized objective function is $J_\mathrm{obj} = J_\mathrm{max}$ (given by expression (3.15)) or $J_\mathrm{obj} = J_\mathrm{diff}$ (given by expression (3.16)).

With objective function (3.19) and parametrization defined as above, the optimization problem can be formulated as

$$\begin{aligned} &\text{Find } \hat{\phi}_* \in \hat{U}_\mathrm{ad} \text{ such that} \\ &J(\hat{\phi}_*) \le J(\hat{\phi}) \quad \forall \hat{\phi} \in \hat{U}_\mathrm{ad}. \end{aligned} \tag{3.20}$$

Recall that the auxiliary function $\hat{\phi}$ gives a level-set function ϕ through smoothing (3.17), and that ϕ in turn determines the design boundary Γ_d through (3.13) and with it the acoustic pressure p^out at the right end of the waveguide, which is used in expressions (3.15) and (3.16).

3.3. Discretization with CutFEM. The fixed-mesh finite element method CutFEM is used to discretize and solve variational problem (3.4) for the acoustic pressure p. Because the mesh is fixed and independent of the design, no remeshing or mesh deformation is needed between design updates. Instead, the design boundary Γ_d is allowed to cut through the elements. The CutFEM approach employed here is similar to the one in [4], and a more detailed description can be found there. Here we take advantage of the rotational symmetry and solve a two-dimensional problem.

The two-dimensional finite element mesh consists of a Cartesian grid of squares, chosen such that the union of elements Ω_h covers the union $\Omega \cup \Omega_\mathrm{d}$. In other words, the mesh domain Ω_h covers the two-dimensional symmetry plane of any admissible design of the compression driver; see Figure 4.

After discretization, variational problem (3.4) takes the form

$$\begin{aligned} &\text{Find } p_h \in V_h, u_\mathrm{m} \in \mathbb{C}, \text{ and } I \in \mathbb{C}, \text{ such that} \\ &A(p_h, q_h) + \epsilon_\mathrm{s} S_h(p_h, q_h) = L(q_h) \quad \forall q_h \in V_h, \\ &\text{and such that the circuit equations (3.2) are satisfied.} \end{aligned} \tag{3.21}$$

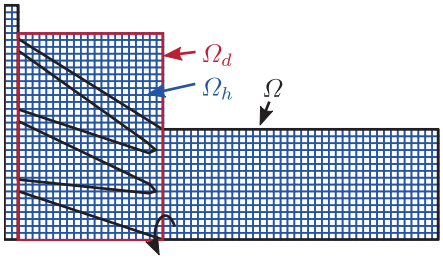

FIG. 4. *An illustration of the mesh, which is structured and fixed. The design boundary Γ_{d} is allowed to cut arbitrarily through the elements. The domain Ω_h equals $\Omega \cup \Omega_{\mathrm{d}}$, so that it covers the computational domain Ω for all admissible designs. Note that the domains Ω and Ω_{d} are the same as in Figure 2, and that the figure is not to scale. Furthermore, note that the rear chamber Ω_{b} is excluded here, since its effect is accounted for by modifying the mechanical impedance Z_{m} as detailed in equation (3.7). The discrete level-set function ϕ and auxiliary function $\hat{\phi}$ are defined in the design domain Ω_{d}, and the inner nodes of Ω_{d} are design nodes: the values $\hat{\phi}_i$ at these nodes are the design variables in optimization problem (3.26).*

Here, A and L are given by (3.5a) and (3.5b), respectively, and S_h is a stabilization term discussed below, with the parameter $\epsilon_{\mathrm{s}} \geq 0$ setting the amount of stabilization. The space of discrete solutions is $V_h = \mathrm{span}\{w_i\}_{i=1}^{N}$, where N is the number of nodes, and the nodal basis functions w_i reduce to the standard two-dimensional biquadratic Lagrange nodal basis functions on each symmetry plane. The finite element solution of the acoustic pressure p_h belongs to V_h and is given by

$$p_h(\boldsymbol{x}) = \sum_{i=1}^{N} p_i w_i(\boldsymbol{x}), \tag{3.22}$$

where p_i is the acoustic pressure at the node located at the point $\boldsymbol{x}_i$.

It is important to note that the nodal value p_i for any node with a neighboring element at least partly inside Ω affects the solution p_h inside Ω, and that, as a consequence, these nodal values are determined by equation (3.21). A consequence of the above is that unfortunate cuts of the elements by the boundary can cause the system matrix to become ill-conditioned. The reason is that the extent to which a nodal value p_i affects the solution p_h inside the domain Ω vanishes as the fraction inside Ω of neighboring elements vanishes. The ill-conditioning is a well-known problem of cut finite element methods, and there are ways to address it [7]. Here we choose to add the stabilization term S_h to discrete variational form (3.21) and define it according to equation (11) in [4]; compare to Burman [6]. The nodal values p_i for nodes with no neighboring element inside Ω can be chosen arbitrarily, and here we simply change the corresponding equations in (3.21) to $p_i = 0$.

3.4. Discrete optimization problem. We follow an approach similar to that in the study on horn optimization in [4] and define a discrete form of optimization problem (3.20). First, the discrete level-set function is defined as

$$\phi_h(\boldsymbol{x}) = \sum_{i=1}^{N^{\mathrm{d}}} \phi_i w_i^{[1]}(\boldsymbol{x}), \tag{3.23}$$

where the nodal basis functions $w_i^{[1]}(\boldsymbol{x})$ reduce to bilinear Lagrange nodal basis functions on each symmetry plane and N^{d} denotes the number of nodes in the design

domain Ω_{d}; see Figure 4. Furthermore, the discrete design boundary Γ_{d}^h in each symmetry plane is defined by linear interpolation between the points where the zero contour of ϕ_h intersects the mesh edges.

Smoothing (3.17) is also carried over to the discrete setting, where the discrete level-set function ϕ_h is given by the discrete auxiliary function $\hat{\phi}_h$, discretized in the same way as ϕ_h, by solving the following variational problem:

$$\begin{aligned} &\text{Find } \phi_h \in V_h^{\mathrm{d}} \text{ such that } \phi_h = \phi_0 \text{ on } \partial\Omega_{\mathrm{d,D}} \text{ and} \\ &A_{\mathrm{d}}(\phi_h, \psi_h) = L_{\mathrm{d}}(\psi_h) \quad \forall \psi_h \in V_h^{\mathrm{d},0}, \end{aligned} \tag{3.24}$$

where

$$A_{\mathrm{d}}(\phi_h, \psi_h) = \int_{\Omega_{\mathrm{d}}} \nabla\psi_h \cdot \nabla\phi_h \,\mathrm{d}\Omega, \tag{3.25a}$$

$$L_{\mathrm{d}}(\psi_h) = \int_{\Omega_{\mathrm{d}}} \psi_h \hat{\phi}_h \,\mathrm{d}\Omega. \tag{3.25b}$$

Here the space of solutions is $V_h^{\mathrm{d},0} = \{\psi_h \in V_h^{\mathrm{d}} : \psi_h = 0 \text{ on } \partial\Omega_{\mathrm{d,D}}\}$ and $V_h^{\mathrm{d}} = \operatorname{span}\{w_i^{[1]}\}_{i=1}^{N^{\mathrm{d}}}$.

We are now ready to formulate the discrete optimization problem:

$$\begin{aligned} &\text{Find } \hat{\phi}_h^* \in V_h^{\mathrm{d},0} \text{ such that} \\ &J(\hat{\phi}_h^*) \le J(\hat{\phi}_h) \quad \forall \hat{\phi}_h \in V_h^{\mathrm{d},0}. \end{aligned} \tag{3.26}$$

Note that the number of design variables equals the number of nodes in the interior of the design domain Ω_{d}; see Figure 4.

The problem of finding the optimal shape of the channels in the compression driver phase plug has now been reformulated as a problem of finding the discrete auxiliary function $\hat{\phi}_h$ (that is, to find its nodal values $\hat{\phi}_i$) that maximizes objective function (3.19). By smoothing (3.24), the function $\hat{\phi}_h$ is mapped to the discrete level-set function ϕ_h, which, by linear interpolation as described above, gives the discrete design boundary Γ_{d}^h and thus the design of the phase plug. The design boundary Γ_{d}^h affects the solution to state equation (3.1) and therefore also the acoustic pressure p_h^{out} at the right end of the waveguide and the objective functions $J_{\max}$ and J_{diff}. The mapping from the nodal values of $\hat{\phi}_i$, from now on referred to as the design parameters, to objective functions $J_{\max}$ and J_{diff} is thus a composite mapping, whereas the mapping from $\hat{\phi}_i$ to regularization term J_ϵ is a quadratic function.

Note that smoothing (3.24) only constitutes a change of variables and that the use of it in itself does not provide any regularization, compared to optimizing over the level-set nodal values ϕ_i directly. It is the inclusion of Tikhonov term (3.18) that provides regularization. However, the change of variables affects the norm, which in turn can affect the steps taken by the optimization algorithm. With smoothing (3.24), one can expect faster convergence when the optimal design is smooth, but possibly slower convergence when, for example, the optimal design is zigzagging. Therefore, the use of smoothing can be viewed as a preconditioning.

3.5. Sensitivity analysis. We use a gradient-based optimization algorithm to solve optimization problem (3.26), since the number of design parameters, the nodal values of the discrete auxiliary function $\hat{\phi}_i$, is large. Consequently, the derivatives of objective function (3.19) with respect to $\hat{\phi}_i$ need to be determined. The central

part of the composite mapping $\hat{\phi}_i \mapsto J$ is the mapping of the level-set function ϕ_h to the acoustic pressure p_h^{out}, and the derivatives of this function can be determined using standard tools of shape sensitivity analysis [11, 38]. Though the derivation is similar to the corresponding analysis in the study of the acoustic horn in [4], there are a couple of essential differences, which are specified below.

The starting point in deriving the discrete derivative $\partial p_h^{\text{out}}/\partial \phi_m$ is to consider a perturbation of the mth nodal value of the level-set function ϕ_h, namely

$$\phi_h(t) = \phi_h + t w_m^{[1]}. \tag{3.27}$$

Here the perturbation is parametrized by $t \geq 0$, and it induces a family of perturbed domains $\Omega_m(t)$, where $t = 0$ gives the unperturbed case.[1] To describe the domain deformation, let us consider a point $\boldsymbol{x} = \boldsymbol{x}(0) \in \Omega = \Omega(0)$, mapped into $\Omega_m(t)$ by $t \mapsto \boldsymbol{x}(t)$, and define the velocity field

$$\boldsymbol{V}_m(\boldsymbol{x}) = \lim_{t \to 0^+} \frac{\boldsymbol{x}(t) - \boldsymbol{x}}{t}. \tag{3.28}$$

The same level-set parametrization is used in the present study and in the previous study on the acoustic horn in [4], and hence the expression for the velocity field derived there [4, equation (A6)] is valid here as well. However, the mesh is defined on the two-dimensional symmetry plane in this paper, and therefore the velocity field is a rotationally symmetric function. The acoustic pressure p_h is also affected by perturbation (3.27), and the *shape derivative* is defined for each $\boldsymbol{x} \in \Omega_h$ as

$$p_h'(0, \boldsymbol{x}) = \lim_{t \to 0^+} \frac{p_h(t, \boldsymbol{x}) - p_h(0, \boldsymbol{x})}{t}, \tag{3.29}$$

where $p_h(t, \boldsymbol{x})$ denotes the solution to state equation (3.1) with Ω replaced by $\Omega_m(t)$.

An essential aspect of the sensitivity analysis when a fixed-mesh finite element method is used (already mentioned in [4]) is that the boundary integral formulation of the discrete derivatives is exact (up to round-off) in this case; when a traditional boundary conforming mesh and mesh deformation are used, however, a domain integral, containing the mesh deformation, must be used to avoid consistency errors [3, 20]. The crucial point is that the shape derivative p_h' belongs to the same finite element space as the discrete solution p_h in the fixed-mesh approach, whereas it does not when mesh deformations are used; in the latter case, it is the so-called material derivative that conforms with the finite element space instead, and the sensitivity analysis must therefore be carried out differently. More details can be found in [4].

In contrast to [4], the solution of an adjoint system of equations is necessary since the output power in the phase plug optimization (at the right end of the waveguide Γ_{out}) and the excitation (at the diaphragm Γ_{m}) are not co-located. The adjoint variational problem is given by

(3.30)

Find $p_h^{\text{adj}} \in V_h, u_{\text{m}}^{\text{adj}} \in \mathbb{C}$, and $I^{\text{adj}} \in \mathbb{C}$, such that

$A(p_h^{\text{adj}}, q_h) = L^{\text{adj}}(q_h) + \epsilon_{\text{s}} S_h(p_h^{\text{adj}}, q_h) \quad \forall q_h \in V_h,$

and such that circuit equations (3.2) are satisfied with $u_{\text{m}} = u_{\text{m}}^{\text{adj}}$ and $V = 0$,

[1] The dependence of $\phi_h(t)$ on m has been suppressed for simplicity of notation.

where

$$L^{\mathrm{adj}}(q_h) = \mathrm{i}kc\rho_0 u_{\mathrm{m}}^{\mathrm{adj}} \int_{\Gamma_{\mathrm{m}}} q_h \,\mathrm{d}\Gamma + 2\mathrm{i}k \int_{\Gamma_{\mathrm{out}}} q_h \,\mathrm{d}\Gamma. \tag{3.31}$$

Note that the voltage in the adjoint problem is zero and that a plane wave source of unit amplitude at Γ_{out} is imposed by the last term in equation (3.31). The driver's motor system (3.2) gives rise to a few additional steps in the derivation in Appendix B, compared to [4].

The expression for the derivative of the acoustic power p_h^{out} at the right end of the waveguide with respect to the level-set function ϕ_h, derived in Appendix B, is

$$\frac{\partial p_h^{\mathrm{out}}}{\partial \phi_m} \coloneqq \lim_{t\to 0^+} \frac{p_h^{\mathrm{out}}(\phi_h(t)) - p_h^{\mathrm{out}}(\phi_h)}{t} = \frac{1}{2\mathrm{i}k|\Gamma_{\mathrm{out}}|} \int_{\Gamma_{\mathrm{d}}^h} \hat{\boldsymbol{n}} \cdot \boldsymbol{V}_m \left(k^2 p_h^{\mathrm{adj}} p_h - \nabla p_h^{\mathrm{adj}} \cdot \nabla p_h \right) \mathrm{d}\Gamma, \tag{3.32}$$

where $\hat{\boldsymbol{n}}$ is the outwards directed unit normal. The derivative of the objective function J with respect to the design variable $\hat{\phi}_i$ is given by

$$\frac{\mathrm{d}J}{\mathrm{d}\hat{\phi}_i} = \frac{\mathrm{d}\phi_m}{\mathrm{d}\hat{\phi}_i} \frac{\mathrm{d}J_{\mathrm{obj}}}{\mathrm{d}\phi_m} + \epsilon_{\mathrm{r}} \frac{\mathrm{d}J_\epsilon}{\mathrm{d}\hat{\phi}_i}, \tag{3.33}$$

where the Einstein summation convention is used. In the discrete case, smoothing (3.17) is a linear function and regularization term (3.18) is a quadratic form, so the corresponding derivative contributions $\mathrm{d}\phi_m/\,\mathrm{d}\hat{\phi}_i$ and $\mathrm{d}J_\epsilon/\,\mathrm{d}\hat{\phi}_i$ are straightforward to compute [4]. As before, the unregularized objective function is $J_{\mathrm{obj}} = J_{\max}$ (given by expression (3.15)) or $J_{\mathrm{obj}} = J_{\mathrm{diff}}$ (given by expression (3.16)); the derivatives of these functions are

$$\frac{\partial J_{\max}}{\partial \phi_m} = -\frac{1}{N_k} \sum_{n=1}^{N_k} \frac{1}{|p_h^{\mathrm{out}}|^2} \mathrm{Re}\left[\frac{\partial p_h^{\mathrm{out}}}{\partial \phi_m} \frac{1}{p_h^{\mathrm{out}}} \right] \text{ and} \tag{3.34a}$$

$$\frac{\partial J_{\mathrm{diff}}}{\partial \phi_m} = \frac{1}{N_k} \sum_{n=1}^{N_k} \mathrm{Re}\left[\frac{\partial p_h^{\mathrm{out}}}{\partial \phi_m} \left(p_h^{\mathrm{out}} - p_{\mathrm{ref}}^{\mathrm{out}} \right)^* \right], \tag{3.34b}$$

respectively.

The derivative expressions (3.32)–(3.34) have been compared to finite difference approximations, with excellent agreement: the maximum absolute relative difference is in the interval $[10^{-8}, 10^{-6}]$ for the different cases. Here, the maximum is taken over the design parameters $\hat{\phi}_i$ or level-set nodal values ϕ_m, as appropriate, and also over wavenumbers k for expression (3.32). Derivatives both for the original design in Figure 4 and a selection of optimized designs have been considered.

It is clear from derivative expression (3.32) that the derivative $\partial p_h^{\mathrm{out}}/\partial \phi_m$ is only nonzero for nodes m for which the design boundary crosses a neighboring element. The same observation applies also to expressions (3.34) for $\partial J_{\max}/\partial \phi_m$ and $\partial J_{\mathrm{diff}}/\partial \phi_m$. However, thanks to the inner derivative $\mathrm{d}\phi_m/\,\mathrm{d}\hat{\phi}_i$ of discrete smoothing (3.24), derivative $\partial J/\partial \hat{\phi}_m$ is in general nonzero for all nodes m (also without Tikhonov regularization, that is, with $\epsilon_{\mathrm{r}} = 0$).

The procedure for solving optimization problem (3.26) can be summarized as follows:

- Set the nodal values $\hat{\phi}_i$ of the discrete auxiliary function $\hat{\phi}_h$ according to the starting design shown in Figure 1. These nodal values $\hat{\phi}_i$ are the design variables.

- In each iteration, do the following until convergence:
  - Compute the level-set function ϕ_h by solving system (3.24).
  - Determine the design boundary Γ_{d}^h.
  - Compute the acoustic pressure p_h by solving (3.21).
  - Compute objective function (3.19) and derivatives (3.33).
  - Update the design variables $\hat{\phi}_i$.

4. Results. The starting point in the optimization is the simplified compression driver design in Figure 1, with three annular channels with positions and relative opening areas as described in section 2. We choose geometrical parameters consistent with a 3-inch compression driver, but with slightly larger diameter to account for the fact that most commercial compression drivers have a domed diaphragm. The diaphragm diameter is 83 mm, the depth of the compression chamber is 0.5 mm, the depth of the rear chamber is 15 mm, the length of the phase plug is 25 mm, the compression ratio is 12, and the diameter of the final waveguide is 38 mm. The mechanical parameters used are suspension compliance $C_{\mathrm{m}} = 20\ \mu\mathrm{m/N}$, moving mass $M_{\mathrm{m}} = 1.3\,\mathrm{g}$, and damping $R_{\mathrm{m}} = 4\,\mathrm{Ns/m}$. The electrical impedance Z_{e} is given by a resistance $R_{\mathrm{e}} = 4\,\Omega$ and an inductance $L_{\mathrm{e}} = 55\,\mu\mathrm{H}$ in series, and the force factor is $Bl = 8\,\mathrm{N/A}$. These values, with the exception of C_{m}, are chosen to be identical to those measured by Makarski [25, p. 10]. However, a larger compliance C_{m} is used here in order to be able to study low frequencies also.

The cut finite element code is implemented in MATLAB. COMSOL Multiphysics is used for verification of the implementation (as described in the last paragraph of subsection 4.1), and we use material parameters for air at equilibrium pressure 1 atm and temperature 20°C from the COMSOL material library for all simulations; this means density $\rho_0 = 1.204\,\mathrm{kg/m^3}$ and speed of sound $c = 343.20\,\mathrm{m/s}$.

The frequency interval considered is chosen to be the four octave band $[0.625, 10]\,\mathrm{kHz}$. The upper frequency bound is chosen so that diaphragm break-up can be considered noncritical. For the waveguide to model an infinite waveguide, it needs to be long enough to let the nonplanar modes decay sufficiently; we choose the length of the waveguide to be 0.5 m, which means that the first nonplanar mode, with cutoff frequency 11.0 kHz, decays with a factor $2 \cdot 10^{-4}$ over twice the length of the waveguide at 10 kHz, and even more for lower frequencies. Note that half a wavelength at 10 kHz is 17.16 mm, which is more than the depth of the rear chamber; consequently, the rear chamber may be accounted for by modifying the mechanical impedance Z_{m} as described in equation (3.7). The lower-frequency bound is chosen so that optimization is at least partly successful, which seems to require the phase plug to be at least one wavelength long; this occurs roughly at 625 Hz when the length of the phase plug is 25 mm.

The discrete geometry is piecewise linear on the finite element mesh, which means that the length of the square mesh elements needs to be small enough to achieve a detailed geometry description. In the numerical experiments reported here, the mesh length is chosen to be 0.25 mm, which is still large enough to keep time and memory consumption low. The stabilization parameter ϵ_{s} in variational formulation (3.21) is set to 0.0025.

To update the geometry, we first tried a quasi-Newton method with the BFGS Hessian update, as implemented in the MATLAB function fminunc. However, in the numerical experiments carried out, this algorithm showed poor convergence. Luckily, as the problem considered is of least-squares type (regardless of whether objective function (3.15) or (3.16) is used), the Levenberg–Marquardt algorithm, implemented

in lsqnonlin in MATLAB, can also be used. This algorithm gives much better convergence for the cases studied here, possibly due to its search direction, which is a mix of the Gauss–Newton and steepest descent directions: The Hessian approximation in the Gauss–Newton method approaches the exact Hessian as the sum of squares approaches zero (that is, close to the optimum), while the steepest descent direction is used to guarantee a descent direction in each step. In the numerical experiments, we noted that smoothing (3.24) did indeed counteract mesh dependence, improve the convergence rate, and promote smooth designs, just as it did in our previous study [4]. All results presented here have been obtained with smoothing (3.24).

4.1. Optimization results. Figure 5 shows optimized phase plug designs and the corresponding sound pressure levels (SPLs) in the waveguide as functions of frequency. The SPL is normalized to an excitation voltage $V = 2\sqrt{2}\,\mathrm{V} = 2\,\mathrm{V}$ RMS in circuit equation (3.2b) and presented in dB-scale, where 0 dB corresponds to $20\,\mu$Pa, to comply with the standard in compression driver data sheets. Here, no regularization was added (that is, $\epsilon_\mathrm{r} = 0$), so objective function (3.19) reduces to (3.15) and (3.16), respectively, both of which are considered. To produce these results, 53 discrete frequencies, logarithmically placed in the interval $[0.625, 10]\,\mathrm{kHz}$, were used. The optimization algorithm successfully decreased the considered objective function; that is, the output power for the discrete set of frequencies is maximized when objective function (3.15) is considered, while the difference to the reference solution is minimized when objective function (3.16) is considered.

For both optimized solutions there are still frequencies in between those used in the optimization where the output power is low. In an attempt to counteract this, the optimization was carried out also using more frequency points, still in the same frequency interval $[0.625, 10]\,\mathrm{kHz}$; the results for the case with 209 frequency points can be found in Figure 6. For these optimized designs, the low-power resonance phenomena are less pronounced, though still present. To alleviate these phenomena, the experiments suggest that it is better to optimize with objective function (3.16), that is, minimize the difference to the ideal solution. The number of iterations needed for the optimization algorithm to converge can also be found Figures 5 and 6. More frequency points in the optimization does not necessarily mean more iterations, but each function evaluation is costlier, since the system of equations must be solved for each frequency. The optimization algorithms terminate when the maximum norm of the discrete gradient is less than 10^{-5} times its initial value, or if the absolute relative change in the objective function between two iterations is less than 10^{-5}.

The phase plug designs in Figures 5 and 6 all show more or less peculiar shapes. Tikhonov regularization is applied in an attempt to control the shape irregularities, since it proved useful in this regard in the study on horn optimization in [4]. A selection of resulting designs, where the difference to the ideal solution is minimized by using objective function (3.19) with $J_\mathrm{obj} = J_\mathrm{diff}$, can be found in Figure 7. We observe that a small amount of regularization, $\epsilon_\mathrm{r} = 10$, results in a design that is similar to the unregularized case, but without some of the short bends. Adding more regularization, $\epsilon_\mathrm{r} = 100$, simplifies the shape of the optimized phase plug even more, which causes the output power to suffer from more pronounced resonance phenomena. The same trend continues as the regularization parameter ϵ_r is increased further.

The cut finite element code is verified by importing the optimized designs into COMSOL Multiphysics and solving the same problem using a very fine boundary-fitted mesh and quadratic elements. The comparison for the two rightmost designs in Figure 7 can be found in Figure 8. The overall agreement is very good, but small

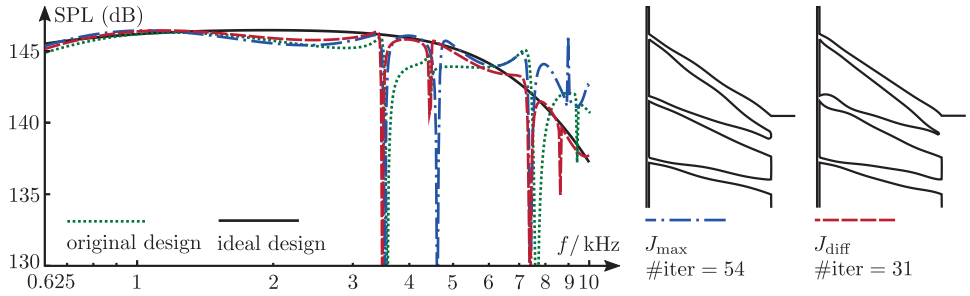

FIG. 5. *Compression driver designs optimized using objective function* $J_{\max}$ *in* (3.15)*, and* J_{diff} *in* (3.16)*, respectively, with* 53 *frequency points. Cuts through the symmetry plane of the optimized drivers are shown to the right, and a graph depicting the sound pressure levels (SPL) in the waveguide is shown to the left. The SPL is normalized to* $20\,\mu$Pa*, for an excitation voltage* $V = 2\sqrt{2}\,\text{V} = 2\,\text{V}$ RMS*, and evaluated at* 417 *frequency points. In the graph, the SPL of the original design in Figure* 1*, as well as the hypothetical ideal driver in Figure* 3*, are also shown.*

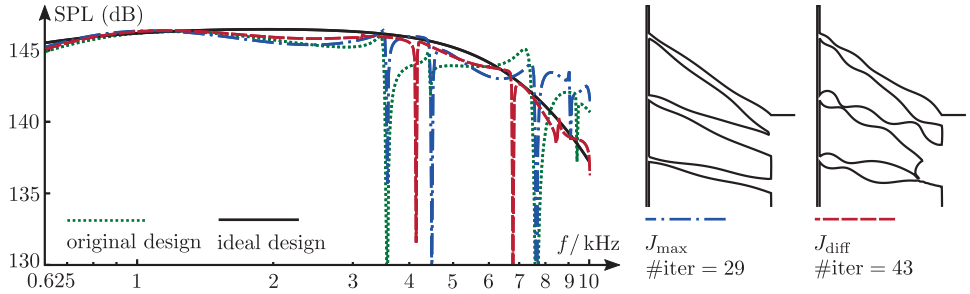

FIG. 6. *Same as Figure* 5*, but using* 209 *frequency points in the optimization.*

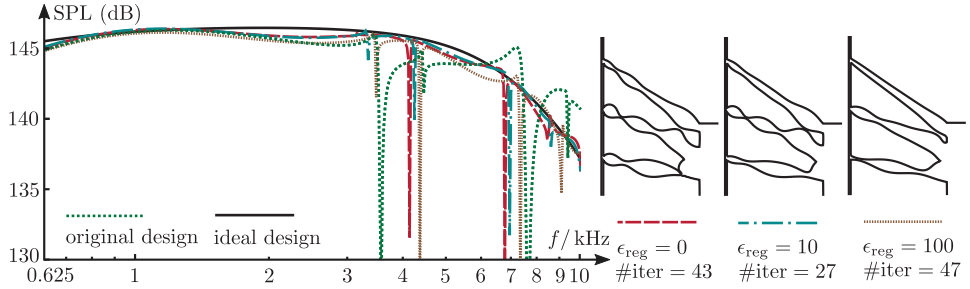

FIG. 7. *Compression driver designs optimized with Tikhonov regularization, that is parameter* $\epsilon_{\text{r}} \neq 0$ *in objective function* (3.19)*, with* $J_{\text{obj}} = J_{\text{diff}}$ *given by* (3.16)*. As in Figure* 6*,* 209 *frequency points were used in the optimization, and the SPL is evaluated at* 417 *frequency points. In the graph, the sound pressure level of the original design and the design found in Figure* 6*, optimized without regularization* ($\epsilon_{\text{r}} = 0$)*, are also shown.*

differences can be observed around the most sensitive frequencies close to the resonance phenomena. These differences are larger for the design with less regularization ($\epsilon_{\text{r}} = 10$), probably because this design has more small features, which are better resolved by the boundary-fitted mesh than the uniform cut finite element mesh. The same observations are made also for the other optimized designs, but, for brevity, the results are not shown explicitly here.

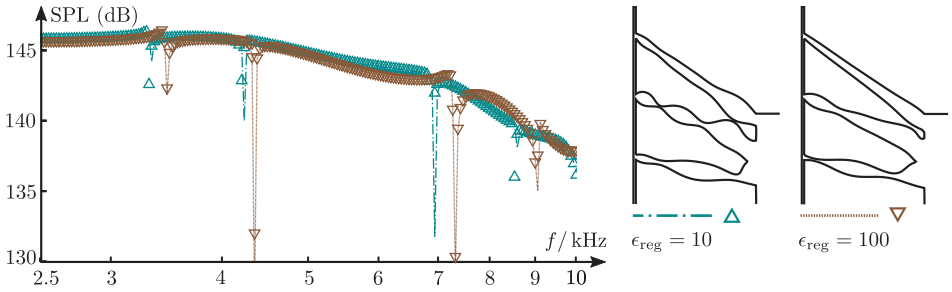

FIG. 8. *The sound pressure level (SPL) computed with the cut finite element code (lines) and Comsol Multiphysics (triangles), respectively, for the two rightmost designs found in Figure 7, that is regularization parameter* $\epsilon_{\text{r}} \neq 0$ *in objective function* (3.19)*, with* $J_{\text{obj}} = J_{\text{diff}}$ *given by* (3.16)*. Note that only the two higher octaves of the frequency interval, that is* $[2.5, 10]$ kHz*, are shown here. In the graph, the SPL was evaluated at* 209 *frequency points.*

4.2. Influence of visco-thermal losses. Acoustic losses caused by viscous and thermal boundary-layer effects are negligible in many applications, but for compression drivers, the high surface to volume ratio due to the narrow chamber and channels means that boundary effects may have a significant impact on the performance [8]. The acoustic losses can accurately be accounted for by solving the linearized Navier–Stokes equation for the pressure, temperature, and velocity fluctuations, rather than the Helmholtz equation (3.1a) for the acoustic pressure only. The extra degrees of freedom, in combination with the fine mesh needed close to the boundary to resolve the high gradients, make the solution computationally much more expensive.

The visco-thermal boundary losses have so far been neglected here, since the computational time for each design iteration would otherwise make optimization infeasible. In this section, however, we present numerical results including losses for some of the optimized designs. With the assumptions that air is an ideal gas with constant viscosity and zero bulk viscosity and that the thermal conductivity is constant, the compressible Navier–Stokes equations, linearized around zero velocity and static pressure, density, and temperature p_0, ρ_0, and T_0, are

$$\mathrm{i}\omega \left(\frac{p}{p_0} - \frac{T}{T_0} \right) \rho + \nabla \cdot \boldsymbol{u} = 0, \tag{4.1a}$$

$$\mathrm{i}\omega \rho_0 \boldsymbol{u} + \nabla p - \mu \left[\Delta \boldsymbol{u} + \frac{1}{3} \nabla (\nabla \cdot \boldsymbol{u}) \right] = \boldsymbol{0}, \tag{4.1b}$$

$$\mathrm{i}\omega \rho_0 c_{\text{p}} T - \mathrm{i}\omega p - \kappa \Delta T = 0, \tag{4.1c}$$

where the fluctuations in pressure, temperature, and velocity are denoted p, T, and $\boldsymbol{u}$, respectively. These equations were solved by using COMSOL Multiphysics, "Thermoviscous Acoustics, Frequency Domain"; compare with the equations on page 439 in COMSOL's *Acoustics Module, User's Guide* [9]. To somewhat reduce the computational burden, we solved the full Navier–Stokes equations in the compression chamber and phase plug and coupled to a solution of the Helmholtz equation in the waveguide, where the losses are negligible. As in the lossless approximation considered previously in the paper, we again used material properties for air at equilibrium pressure $p_0 = 1\,\text{atm}$ and temperature $T_0 = 20^\circ\text{C}$ from the COMSOL material library, which means density $\rho_0 = 1.204\,\text{kg/m}^3$, dynamic viscosity $\mu = 1.8140 \cdot 10^{-5}\,\text{Pa} \cdot \text{s}$, specific heat at constant pressure $c_{\text{p}} = 1.0054 \cdot 10^3\,\text{J/(kg} \cdot \text{K)}$, and thermal conductivity $\kappa = 2.5768 \cdot 10^{-2}\,\text{W/(m} \cdot \text{K)}$.

Numerical results when losses are included for the designs in Figure 7 can be found in Figure 9. As expected, it is seen that the output power for most frequencies is reduced compared to the lossless case. The frequency irregularities are somewhat alleviated by the losses; the dips in output power are wider, less deep, and slightly shifted down in frequency. Furthermore, the optimized designs clearly outperform the original design.

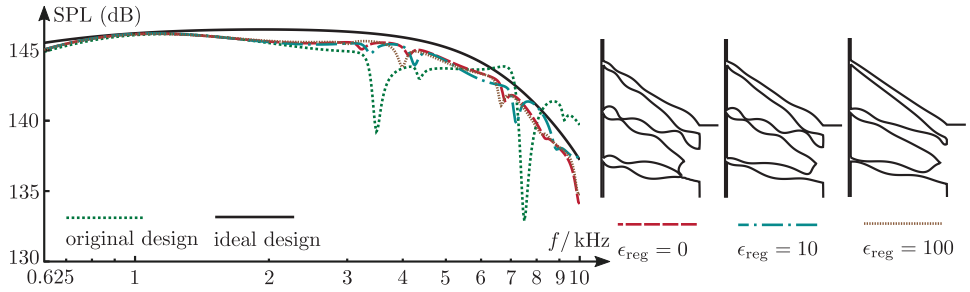

FIG. 9. *The sound pressure level (SPL) computed by solving the linearized, compressible Navier–Stokes equations* (4.1) *to account for viscous and thermal boundary-layer losses, for the optimized designs found in Figure* 7*, that is using objective function* (3.19) *with varying regularization parameter* ϵ_{r} *and with* $J_{\text{obj}} = J_{\text{diff}}$ *given by* (3.16)*. The sound pressure level for the original design, also including losses, and the lossless hypothetical ideal design are also shown for reference. The SPL is normalized as in the previous figures, that is with excitation voltage* $V = 2\sqrt{2}\,\text{V} = 2\,\text{V}$ RMS *and with 0 dB corresponding to* $20\,\mu\text{Pa}$*, and evaluated at* 417 *frequency points.*

5. Conclusions. We propose using a level-set based optimization procedure for compression driver phase plug design, where the filtered nodal values of the discrete level-set function are used as design variables to provide a large design freedom. The shapes of the optimized phase plugs in the numerical experiments are, as far as we know, not similar to any existing design, and would have been hard to find by a manual design process or optimization methods constrained to a geometry parametrization with a few parameters. The output sound pressure levels (SPLs) of the optimized designs contain only minor frequency irregularities and are very close to the SPL of the hypothetical ideal design with separated output channels. Moreover, we find that minimizing the difference in output to the ideal design is more successful in achieving a smooth frequency response, compared to maximizing SPL. The proposed method is robust and computationally cheap, thanks to the CutFEM discretization on a fixed mesh; apart from removing the need for mesh modification during the design iterations, the fixed-mesh method also implies that the discrete design shape sensitivities are given by boundary integrals rather than volume integrals, which are computationally more expensive to evaluate.

The numerical experiments show that the introduction of visco-thermal boundary-layer losses in the model makes the dips in output SPL wider, less deep, and slightly shifted down in frequency. The optimized designs clearly outperform the original design also when these losses are accounted for, but it is not clear whether the optimized designs would differ significantly should these mechanisms be included during the optimization. Thin air gaps, which are where the boundary-layer losses primarily originate, might then become less common. The addition of Tikhonov regularization in the numerical experiments reduces the prevalence of thin gaps somewhat, though with little effect on the computed SPL; the boundary-layer losses in the compression chamber itself probably exceed the losses in the phase plug.

The focus of our study is phase plug design, and our analysis is therefore constrained to the frequency range where diaphragm break-up can be assumed to have negligible effect. Optimizing compression drivers for higher frequencies, where diaphragm break-up is likely to occur, is a very challenging multiphysics problem where the phase plug and diaphragm need to be co-optimized. Finally, it should be mentioned that there are no conceptual differences in applying the proposed method to optimize phase plugs for compression drivers with noncylindrical compression chambers. Phase plugs lacking rotational symmetry can also be optimized with the method, although this inevitably makes the solution computationally more expensive.

Appendix A. Well-posedness. The arguments below rely on standard Fredholm theory, and traces on parts of the boundary are needed for Lemma A.2 and Theorem A.3, which is why we here make the explicit assumption that the domain is open, bounded, connected, and provided with a Lipschitz boundary. Throughout this appendix, Re and Im denote the real and imaginary parts, respectively, and an asterisk (*) denotes the complex conjugate. For convenience, we define the effective admittance $Y_{\text{eff}} = Z_{\text{eff}}^{-1}$, where Z_{eff} is given by (3.12). Note that $\operatorname{Re} Y_{\text{eff}} > 0 \Leftrightarrow \operatorname{Re} Z_{\text{eff}} > 0$. We show coercivity and injectivity in the following two lemmas, and with these results we show well-posedness in Theorem A.3.

LEMMA A.1 (coercivity). *Assume that* $\operatorname{Re} Y_{\text{eff}} > 0$. *Then, for any* $p \in H^1(\Omega)$,

$$\left| A'(p,p^*) + 2k^2 \int_\Omega |p|^2 \,\mathrm{d}\Omega \right| \geq \left[1 + 4 \left(\frac{|\operatorname{Im} Y_{\text{eff}}|}{\operatorname{Re} Y_{\text{eff}}} \right)^2 \right]^{-\frac{1}{2}} \left(\int_\Omega |\nabla p|^2 \,\mathrm{d}\Omega + k^2 \int_\Omega |p|^2 \,\mathrm{d}\Omega \right).$$

Proof.

$$\begin{aligned}
&\sqrt{1 + 4 \left(\frac{|\operatorname{Im} Y_{\text{eff}}|}{\operatorname{Re} Y_{\text{eff}}} \right)^2} \left| A'(p,p^*) + 2k^2 \int_\Omega |p|^2 \,\mathrm{d}\Omega \right| \\
&\geq \operatorname{Re} \left[\left(1 - \mathrm{i}2 \frac{|\operatorname{Im} Y_{\text{eff}}|}{\operatorname{Re} Y_{\text{eff}}} \right) \left(A'(p,p^*) + 2k^2 \int_\Omega |p|^2 \,\mathrm{d}\Omega \right) \right] \\
&= \int_\Omega |\nabla p|^2 \,\mathrm{d}\Omega + k^2 \int_\Omega |p|^2 \,\mathrm{d}\Omega + 2 \frac{|\operatorname{Im} Y_{\text{eff}}|}{\operatorname{Re} Y_{\text{eff}}} k \int_{\Gamma_{\text{out}}} |p|^2 \,\mathrm{d}\Gamma + (2|\operatorname{Im} Y_{\text{eff}}| - \operatorname{Im} Y_{\text{eff}}) kc\rho_0 \left| \int_{\Gamma_{\text{m}}} p \,\mathrm{d}\Gamma \right|^2 \\
&\geq \int_\Omega |\nabla p|^2 \,\mathrm{d}\Omega + k^2 \int_\Omega |p|^2 \,\mathrm{d}\Omega.
\end{aligned}$$

∎

LEMMA A.2 (injectivity). *Assume that* $\operatorname{Re} Y_{\text{eff}} \geq 0$. *Then, for each* $k > 0$, *if* $p \in H^1(\Omega)$ *such that*

$$A'(p,q) = 0 \qquad \forall q \in H^1(\Omega), \tag{A.1}$$

it holds that $p = 0$.

Proof. Assume that p satisfies (A.1), and consider

$$0 = \operatorname{Im} A'(p,p^*) = k \int_{\Gamma_{\text{out}}} |p|^2 \,\mathrm{d}\Gamma + kc\rho_0 \operatorname{Re} Y_{\text{eff}} \left| \int_{\Gamma_{\text{m}}} p \,\mathrm{d}\Gamma \right|^2. \tag{A.2}$$

Since $\operatorname{Re} Y_{\text{eff}} \geq 0$, expression (A.2) implies that p vanishes on Γ_{out}, which implies that it can be continuously extended by zero into a region with positive measure outside of Γ_{out}. Denote the extended domain $\hat{\Omega}$. It holds for the extended function that

$p \in H^1(\hat{\Omega})$. Since p satisfies equation (A.1), vanishes on $\hat{\Omega} \setminus \Omega$, and is continuous across Γ_{out}, it follows that

$$\int_K \nabla p \cdot \nabla q - k^2 \int_K qp = 0 \qquad \forall q \in C_0^\infty(K), \tag{A.3}$$

for each open set K compactly embedded in $\hat{\Omega}$, which implies, by the definition of weak derivative, that almost everywhere in K,

$$\Delta p + k^2 p = 0. \tag{A.4}$$

Since p satisfies equation (A.4) and vanishes on $\hat{\Omega} \setminus \Omega$, the unique continuation principle [23, section 4.3] implies that p vanishes on $\hat{\Omega}$. ∎

THEOREM A.3. *Problem* (3.10) *is well-posed for each* $k > 0$ *under the assumption that* $\operatorname{Re} Z_{\text{eff}} > 0$.

Proof. The Cauchy–Schwarz inequality and Lemma A.1 imply that bilinear form (3.11a) is continuous and coercive. Since the domain Ω is bounded, the natural injection of $H^1(\Omega)$ into $L^2(\Omega)$ is compact. The solution theory for elliptic variational problems, as formulated, for instance, by Wloka [45, Thm. 17.11], then yields that either the homogeneous problem, equation (3.10) with $L' = 0$, has a nontrivial solution, or A' constitutes an isomorphism of $H^1(\Omega)$ onto its dual. However, Lemma A.2 shows that the homogeneous problem only has the trivial solution. Since L' is bounded on $H^1(\Omega)$ by the trace theorem on $H^1(\Omega)$ [45, Thm. 8.7], problem (3.10) is well-posed. ∎

Appendix B. Details on the sensitivity analysis. Here, expression (3.32) for the discrete derivative of the pressure p_h^{out} with respect to the level-set nodal values $\hat{\phi}_i$ is derived. The shape derivative $p_h'(t)$ of the acoustic pressure $p_h(t)$ was defined in expression (3.29), and the shape derivative of any family of functions $\psi(t)$ on the perturbed domain $\Omega_m(t)$ is defined analogously. We will also need the following classical result for the derivative of a domain integral $F_m(t;\psi) = \int_{\Omega_m(t)} \psi(t)\,\mathrm{d}\Omega$:

$$\mathrm{d}F_m(0;\psi) \overset{\text{def}}{=} \lim_{t\to 0^+} \frac{1}{t}\left(\int_{\Omega_m(t)} \psi(t)\,\mathrm{d}\Omega - \int_\Omega \psi(0)\,\mathrm{d}\Omega\right) = \int_\Omega \left[\psi'(0) + \nabla\cdot(\boldsymbol{V}_m\psi(0))\right]\mathrm{d}\Omega, \tag{B.1}$$

where the second equality holds, for example, if ψ, ψ', and $\nabla\psi$ are in $L^1(\Omega)$, and if $\boldsymbol{V}_m$ is in $C^1(\Omega)$ [11, Ch. 9, section 4.1].

To derive expression (3.32) for the derivative

$$\frac{\partial p_h^{\text{out}}}{\partial \phi_m} = \frac{1}{|\Gamma_{\text{out}}|}\int_{\Gamma_{\text{out}}} p_h'\,\mathrm{d}\Gamma, \tag{B.2}$$

we study the perturbation of variational form (3.21) with respect to the velocity $\boldsymbol{V}_m$ corresponding to perturbation (3.27). For simplicity, the case without stabilization (that is, $\epsilon_{\text{s}} = 0$) is treated first, but including stabilization makes no major difference in the derivations. As we will see, the case when the level set vanishes at the considered node, $\phi_m = 0$, is special, and therefore we start by considering the case $\phi_m \neq 0$. All integrals over the domain Ω_h are written as sums over the elements T in the mesh $\mathcal{T}_h$, to make use of the fact that the restriction of p_h and $\boldsymbol{V}_m$ on each such intersection are polynomials, so that the classical derivative expression (B.1) can be

used. Let $A_m(t;\cdot,\cdot)$ and $L_m(t;\cdot)$ denote bilinear form (3.5a) and linear form (3.5b), respectively, with Ω replaced by $\Omega_m(t)$. After reordering, the derivative of variational form (3.21) can be written

$$\begin{aligned}
0 &= \mathrm{d}A_m(0;p_h,q_h) - \mathrm{d}L_m(0;q_h)\\
&= \sum_{T\in\mathcal{T}_h}\int_{T\cap\Omega}\left(\nabla q_h'\cdot\nabla p_h - k^2 q_h' p_h\right)\mathrm{d}\Omega + \mathrm{i}k\int_{\Gamma_{\mathrm{out}}} q_h' p_h\,\mathrm{d}\Gamma - \mathrm{i}kc\rho_0 u_{\mathrm{m}}\int_{\Gamma_{\mathrm{m}}} q_h'\,\mathrm{d}\Gamma\\
&+ \sum_{T\in\mathcal{T}_h}\int_{T\cap\Omega}\left(\nabla q_h\cdot\nabla p_h' - k^2 q_h p_h'\right)\mathrm{d}\Omega + \mathrm{i}k\int_{\Gamma_{\mathrm{out}}} q_h p_h'\,\mathrm{d}\Gamma - \mathrm{i}kc\rho_0 u_{\mathrm{m}}'\int_{\Gamma_{\mathrm{m}}} q_h\,\mathrm{d}\Gamma\\
&+ \sum_{T\in\mathcal{T}_h}\int_{T\cap\Omega}\nabla\cdot\left(\boldsymbol{V}_m\nabla q_h\cdot\nabla p_h - \boldsymbol{V}_m k^2 q_h p_h\right)\mathrm{d}\Omega, \qquad \text{(B.3)}
\end{aligned}$$

where, in the second equality, we have used the product rule and that shape differentiation commutes with the gradient operator. Moreover, since q_h' belongs to V_h and p_h satisfies variational problem (3.21), we find that the terms containing q_h' sum up to zero.

Remark B.1. As mentioned in section 3.5, that the shape derivative q_h' of a function $q_h \in V_h$ remains in V_h is a consequence of our use of a fixed mesh. This property does not hold when traditional boundary-conforming mesh and mesh-deformation strategies are used.

Since the solution p_h^{adj} to adjoint variational problem (3.30) belongs to the finite element space V_h, it can be used in place of q_h in (B.3) to get

$$\begin{aligned}
&\sum_{T\in\mathcal{T}_h}\int_{T\cap\Omega}\nabla\cdot\left(\boldsymbol{V}_m k^2 p_h^{\mathrm{adj}} p_h - \boldsymbol{V}_m\nabla p_h^{\mathrm{adj}}\cdot\nabla p_h\right)\mathrm{d}\Omega\\
&= A(p_h', p_h^{\mathrm{adj}}) - \mathrm{i}kc\rho_0 u_{\mathrm{m}}'\int_{\Gamma_{\mathrm{m}}} p_h^{\mathrm{adj}}\,\mathrm{d}\Gamma.
\end{aligned} \qquad \text{(B.4)}$$

Now, make the choice $q_h = p_h' \in V_h$ in adjoint variational problem (3.30) to get

$$\mathrm{i}kc\rho_0 u_{\mathrm{m}}^{\mathrm{adj}}\int_{\Gamma_{\mathrm{m}}} p_h'\,\mathrm{d}\Gamma + 2\mathrm{i}k\int_{\Gamma_{\mathrm{out}}} p_h'\,\mathrm{d}\Gamma = L^{\mathrm{adj}}(p_h') = A(p_h', p_h^{\mathrm{adj}}). \qquad \text{(B.5)}$$

Combining expressions (B.4) and (B.5) gives

$$\begin{aligned}
&\sum_{T\in\mathcal{T}_h}\int_{T\cap\Omega}\nabla\cdot\left(\boldsymbol{V}_m k^2 p_h^{\mathrm{adj}} p_h - \boldsymbol{V}_m\nabla p_h^{\mathrm{adj}}\cdot\nabla p_h\right)\mathrm{d}\Gamma\\
&= \mathrm{i}kc\rho_0 u_{\mathrm{m}}^{\mathrm{adj}}\int_{\Gamma_{\mathrm{m}}} p_h'\,\mathrm{d}\Gamma + 2\mathrm{i}k\int_{\Gamma_{\mathrm{out}}} p_h'\,\mathrm{d}\Gamma - \mathrm{i}kc\rho_0 u_{\mathrm{m}}'\int_{\Gamma_{\mathrm{m}}} p_h^{\mathrm{adj}}\,\mathrm{d}\Gamma.
\end{aligned} \qquad \text{(B.6)}$$

Circuit equation (3.2a) followed by (3.2b) gives

$$\int_{\Gamma_{\mathrm{m}}}[\![p_h]\!]'\,\mathrm{d}\Gamma = BlI' - Z_{\mathrm{m}}u_{\mathrm{m}}' = \left(\frac{B^2l^2}{Z_{\mathrm{m}}} - Z_{\mathrm{m}}\right)u_{\mathrm{m}}' \text{ and} \qquad \text{(B.7a)}$$

$$\int_{\Gamma_{\mathrm{m}}}[\![p_h^{\mathrm{adj}}]\!]\,\mathrm{d}\Gamma = BlI^{\mathrm{adj}} - Z_{\mathrm{m}}u_{\mathrm{m}}^{\mathrm{adj}} = \left(\frac{B^2l^2}{Z_{\mathrm{m}}} - Z_{\mathrm{m}}\right)u_{\mathrm{m}}^{\mathrm{adj}}. \qquad \text{(B.7b)}$$

Here $[\![p_h]\!] = p_h|_{\Gamma_\mathrm{m}} - p_\mathrm{b}|_{\Gamma_\mathrm{m}}$, and p_h (p_b) denotes the pressure in Ω (Ω_b), and likewise for p_h^adj. Note that the geometry of the back chamber is fixed, which implies that there is a constant $C \in \mathbb{C}$ such that

$$\int_{\Gamma_\mathrm{m}} p_\mathrm{b}' \,\mathrm{d}\Gamma = C u_\mathrm{m}' \text{ and } \int_{\Gamma_\mathrm{m}} p_\mathrm{b}^\mathrm{adj} \,\mathrm{d}\Gamma = C u_\mathrm{m}^\mathrm{adj}. \tag{B.8}$$

Equations (B.7a) and (B.7b) therefore imply that the first and last terms on the right-hand side of equation (B.6) cancel; by using expression (B.2) on the remaining term, we find that

$$\frac{1}{2\mathrm{i}k|\Gamma_\mathrm{out}|} \sum_{T\in\mathcal{T}_h} \int_{T\cap\Omega} \nabla\cdot\Big(\boldsymbol{V}_m k^2 p_h^\mathrm{adj} p_h - \boldsymbol{V}_m \nabla p_h^\mathrm{adj}\cdot\nabla p_h\Big)\,\mathrm{d}\Omega = \frac{\partial p_h^\mathrm{out}}{\partial \phi_m}. \tag{B.9}$$

Finally, the divergence theorem can be used to rewrite each integral in the sum on the left-hand side as a boundary integral, since the integrand is a polynomial and the restriction of each intersection $T \cap \Omega$ to any symmetry plane is a polygon. In [4], it is shown that the velocity field vanishes or is tangent to the polygon edges that are not part of the design boundary Γ_d^h, so expression (B.9) simplifies to

$$\frac{\partial p_h^\mathrm{out}}{\partial \phi_m} = \frac{1}{2\mathrm{i}k|\Gamma_\mathrm{out}|} \int_{\Gamma_\mathrm{d}^h} \hat{\boldsymbol{n}}\cdot\boldsymbol{V}_m \Big(k^2 p_h^\mathrm{adj} p_h - \nabla p_h^\mathrm{adj}\cdot\nabla p_h\Big)\,\mathrm{d}\Gamma, \tag{B.10}$$

which proves expression (3.32).

It remains to consider the case when $\phi_m = 0$, in which case the function $t \mapsto p_h^\mathrm{out}$ is not differentiable; its right and left derivatives do not coincide. There are two cases to consider: The first occurs when the design boundary crosses node m, that is, when there are both neighboring nodes where the level set is positive and those where it is negative. In this case, we choose the right derivative, as indicated in equation (3.32). The other case could occur in the rare instance when the level-set function vanishes at node m and is positive at all neighboring nodes or negative at all neighboring nodes. In this case, the right (left) derivative is zero when the neighboring nodes are positive (negative), whereas the left (right) derivative takes into account the insertion of an island of material (void). We do not aim for topological changes here and therefore consider these derivatives to be equal to zero.

Including the stabilization term $\epsilon_\mathrm{s} S_h(p_h, q_h)$ in state equation (3.21) does not change expression (3.32) as long as the design boundary Γ_d^h does not cross any mesh node, as described in [4]. However, when Γ_d^h does cross the mth mesh node, the function $t \mapsto S_h(p_h, q_h)$ will not be continuous at zero. Nonetheless, we use equation (3.32) also when the design boundary crosses a mesh node, since the effect of the non-differentiability of the stabilization term is expected to be negligible for moderate amounts of stabilization.

Acknowledgment. The computations were performed on resources provided by the Swedish National Infrastructure for Computing (SNIC) at the High Performance Computing Center North (HPC2N).

REFERENCES

[1] E. Bängtsson, D. Noreland, and M. Berggren, *Shape optimization of an acoustic horn*, Comput. Methods Appl. Mech. Engrg., 192 (2003), pp. 1533–1571, https://doi.org/10.1016/S0045-7825(02)00656-4.

[2] R. Barbieri and N. Barbieri, *Acoustic horns optimization using finite elements and genetic algorithm*, Appl. Acoust., 74 (2013), pp. 356–363, https://doi.org/10.1016/j.apacoust.2012.09.007.

[3] M. Berggren, *A unified discrete–continuous sensitivity analysis method for shape optimization*, in Applied and Numerical Partial Differential Equations: Scientific Computing in Simulation, Optimization and Control in a Multidisciplinary Context, Springer, Dordrecht, The Netherlands, 2010, pp. 25–39, https://doi.org/10.1007/978-90-481-3239-3_4.

[4] A. Bernland, E. Wadbro, and M. Berggren, *Acoustic shape optimization using cut finite elements*, Internat. J. Numer. Methods Engrg., 113 (2018), pp. 432–449, https://doi.org/10.1002/nme.5621.

[5] M. Burger and S. J. Osher, *A survey on level set methods for inverse problems and optimal design*, European J. Appl. Math, 16 (2005), pp. 263–301.

[6] E. Burman, *Ghost penalty*, C. R. Math. Acad. Sci. Paris, 348 (2010), pp. 1217–1220, https://doi.org/10.1016/j.crma.2010.10.006.

[7] E. Burman, S. Claus, P. Hansbo, M. G. Larson, and A. Massing, *CutFEM: Discretizing geometry and partial differential equations*, Internat. J. Numer. Methods Engrg., 104 (2015), pp. 472–501, https://doi.org/10.1002/nme.4823.

[8] R. Christensen and U. Skov, *Simulation of a 4″ compression driver using a fully coupled vibroacoustic finite element analysis including viscous and thermal losses*, in Audio Engineering Society Convention 132, 2012, 8672, http://www.aes.org/e-lib/browse.cfm?elib=16310.

[9] Comsol, Inc., *COMSOL Multiphysics Version* 5.3*, Acoustics Module, User's Guide*, COMSOL, Inc., Burlington, MA, 2017.

[10] J. D. Deaton and R. V. Grandhi, *A survey of structural and multidisciplinary continuum topology optimization: Post* 2000, Struct. Multidiscip. Optim., 49 (2014), pp. 1–38, https://doi.org/10.1007/s00158-013-0956-z.

[11] M. C. Delfour and J.-P. Zolézio, *Shapes and Geometries. Metrics, Analysis, Differential Calculus, and Optimization*, 2nd ed., SIAM, Philadelphia, 2011, https://doi.org/10.1137/1.9780898719826.

[12] M. Dodd, *The development of a forward radiating compression driver by the application of acoustic, magnetic and thermal finite element methods*, in Audio Engineering Society Convention 115, 2003, 5886, http://www.aes.org/e-lib/browse.cfm?elib=12445.

[13] M. Dodd, *Wideband compression driver design, part* 2*: Application to a high power compression driver with a novel diaphragm geometry*, in Audio Engineering Society Convention 139, 2015, 9391, http://www.aes.org/e-lib/browse.cfm?elib=17948.

[14] M. Dodd and J. Oclee-Brown, *A new methodology for the acoustic design of compression driver phase-plugs with concentric annular channels*, in Audio Engineering Society Convention 123, 2007, 7258, http://www.aes.org/e-lib/browse.cfm?elib=14316.

[15] B. Farhadinia, *Structural optimization of an acoustic horn*, Appl. Math. Model., 36 (2012), pp. 2017–2030, https://doi.org/10.1016/j.apm.2011.08.016.

[16] T.-P. Fries and T. Belytschko, *The extended/generalized finite element method: An overview of the method and its applications*, Internat. J. Numer. Methods Engrg., 84 (2010), pp. 253–304, https://doi.org/10.1002/nme.2914.

[17] A. L. Gain and G. H. Paulino, *A critical comparative assessment of differential equation-driven methods for structural topology optimization*, Struct. Multidiscip. Optim., 48 (2013), pp. 685–710, https://doi.org/10.1007/s00158-013-0935-4.

[18] M. Gasparini, S. Cecchi, F. Piazza, E. Capucci, and R. Toppi, *Multiphysic modeling and heuristic optimization of compression driver design*, in Audio Engineering Society Convention 136, 2014, 9069, http://www.aes.org/e-lib/browse.cfm?elib=17216.

[19] C. R. Hanna and J. Slepian, *The function and design of horns for loud speakers*, Trans. Amer. Inst. Electrical Engineers, 43 (1924), pp. 393–411, https://doi.org/10.1109/T-AIEE.1924.5060995.

[20] R. Hiptmair, A. Paganini, and S. Sargheini, *Comparison of approximate shape gradients*, BIT, 55 (2015), pp. 459–485, https://doi.org/10.1007/s10543-014-0515-z.

[21] F. Kasolis, E. Wadbro, and M. Berggren, *Fixed-mesh curvature-parameterized shape optimization of an acoustic horn*, Struct. Multidiscip. Optim., 46 (2012), pp. 727–738, https://doi.org/10.1007/s00158-012-0828-y.

[22] A. Legay, *An extended finite element method approach for structural-acoustic problems involving immersed structures at arbitrary positions*, Internat. J. Numer. Methods Engrg., 93 (2013), pp. 376–399, https://doi.org/10.1002/nme.4388.

[23] R. Leis, *Initial Boundary Value Problems in Mathematical Physics*, Dover, New York, 2013.

[24] L. Li, M. Y. Wang, and P. Wei, *XFEM schemes for level set based structural optimization*, Frontiers Mech. Engrg., 7 (2012), pp. 335–356, https://doi.org/10.1007/s11465-012-0351-2.

[25] M. Makarski, *Tools for the Professional Development of Horn Loudspeakers*, Ph.D. thesis, Rheinisch-Westfälischen Technischen Hochschule Aachen, Aachen, Germany, 2006, http://publications.rwth-aachen.de/record/61507.

[26] D. Makhija and K. Maute, *Numerical instabilities in level set topology optimization with the extended finite element method*, Struct. Multidiscip. Optim., 49 (2014), pp. 185–197, https://doi.org/10.1007/s00158-013-0982-x.

[27] R. C. Morgans, A. C. Zander, C. H. Hansen, and D. J. Murphy, *EGO shape optimization of horn-loaded loudspeakers*, Optim. Engrg., 9 (2008), pp. 361–374, https://doi.org/10.1007/s11081-007-9029-8.

[28] D. J. Munk, G. A. Vio, and G. P. Steven, *Topology and shape optimization methods using evolutionary algorithms: A review*, Struct. Multidiscip. Optim., 52 (2015), pp. 613–631, https://doi.org/10.1007/s00158-015-1261-9.

[29] D. R. Noble, E. P. Newren, and J. B. Lechman, *A conformal decomposition finite element method for modeling stationary fluid interface problems*, Internat. J. Numer. Methods Fluids, 63 (2010), pp. 725–742, https://doi.org/10.1002/fld.2095.

[30] D. Noreland, R. Udawalpola, P. Seoane, E. Wadbro, and M. Berggren, *An Efficient Loudspeaker Horn Designed by Numerical Optimization: An Experimental Study*, Tech. Report UMINF 10.1, Umeå University, Department of Computing Science, Umeå, Sweden, 2010; available online from http://www.cs.umu.se.

[31] J. Oclee-Brown, *Loudspeaker Compression-Driver Phase-Plug Design*, Ph.D. thesis, University of Southampton, Southampton, UK, 2012, https://eprints.soton.ac.uk/348798/.

[32] J. Oclee-Brown, *A general approach for the acoustic design of compression drivers with "narrow" channels and rigid diaphragms*, in Audio Engineering Society Convention 137, 2014, 9165, http://www.aes.org/e-lib/browse.cfm?elib=17488.

[33] J. Oclee-Brown, *Wideband compression driver design, part* 1: *A theoretical approach to designing compression drivers with non-rigid diaphragms*, in Audio Engineering Society Convention 139, 2015, 9386, http://www.aes.org/e-lib/browse.cfm?elib=17943.

[34] S. Schmidt, E. Wadbro, and M. Berggren, *Large-scale three-dimensional acoustic horn optimization*, SIAM J. Sci. Comput., 38 (2016), pp. B917–B940, https://doi.org/10.1137/15M1021131.

[35] O. Sigmund and K. Maute, *Topology optimization approaches*, Struct. Multidiscip. Optim., 48 (2013), pp. 1031–1055, https://doi.org/10.1007/s00158-013-0978-6.

[36] B. H. Smith, *An investigation of the air chamber of horn type loudspeakers*, J. Acoust. Soc. Amer., 25 (1953), pp. 305–312, https://doi.org/10.1121/1.1907038.

[37] S. Soghrati, A. M. Aragón, C. Armando Duarte, and P. H. Geubelle, *An interface-enriched generalized FEM for problems with discontinuous gradient fields*, Internat. J. Numer. Methods Engrg., 89 (2012), pp. 991–1008, https://doi.org/10.1002/nme.3273.

[38] J. Sokolowski and J.-P. Zolesio, *Introduction to Shape Optimization*, Springer, Berlin, Heidelberg, 1992, https://doi.org/10.1007/978-3-642-58106-9_1.

[39] N. P. van Dijk, K. Maute, M. Langelaar, and F. van Keulen, *Level-set methods for structural topology optimization: A review*, Struct. Multidiscip. Optim., 48 (2013), pp. 437–472, https://doi.org/10.1007/s00158-013-0912-y.

[40] L. Van Miegroet and P. Duysinx, *Stress concentration minimization of* 2*D filets using X-FEM and level set description*, Struct. Multidiscip. Optim., 33 (2007), pp. 425–438, https://doi.org/10.1007/s00158-006-0091-1.

[41] C. H. Villanueva and K. Maute, *Density and level set-XFEM schemes for topology optimization of* 3*-D structures*, Comput. Mech., 54 (2014), pp. 133–150, https://doi.org/10.1007/s00466-014-1027-z.

[42] A. Voishvillo, *Compression drivers' phasing plugs*, in Audio Engineering Society Convention 141, 2016, 9618, http://www.aes.org/e-lib/browse.cfm?elib=18422.

[43] P. Wei, M. Y. Wang, and X. Xing, *A study on X-FEM in continuum structural optimization using a level set model*, Comput.-Aided Des., 42 (2010), pp. 708–719, https://doi.org/10.1016/j.cad.2009.12.001.

[44] E. C. Wente and A. L. Thuras, *A high efficiency receiver for a horn-type loud speaker of large power capacity*, Bell Syst. Tech. J., 7 (1928), pp. 140–153, https://doi.org/10.1002/j.1538-7305.1928.tb00344.x.

[45] J. Wloka, *Partial Differential Equations*, Cambridge University Press, Cambridge, UK, 1987.